https://dx.doi.org/10.1016/j.ijsolstr.2020.05.004

Exploring the effect of particle shape caused by erosion on the shear behaviour of granular materials via the DEM

Authors: Zhihong Nie[a], Chuanfeng Fang[a], Jian Gong[b*], Zhenyu Yin[c]

a School of Civil Engineering, Central South University, Changsha, Hunan 410075, China

b School of Hydraulic Engineering, Changsha Univerisity of Science and Technology, Changsha 410114, China

c Department of Civil and Environmental Engineering, The Hong Kong Polytechnic University, Hong Kong, China

[*] Corresponding author. Email: gj_csu@hotmail.com

Abstract:

The fragments from crushed rock are initially very angular. The erosion process causes the fragment shape to evolve from angular to well rounded and affects the mechanical behaviour of granular materials. This report explores the effect of particle shape caused by erosion (E_r) on macroscopic and microscopic behaviour under triaxial compression tests of granular materials via the discrete element method. A convex rigid block was employed to model particles with different erosion degrees. After being prepared in the densest condition, all particle assemblies were subjected to axial compression until a critical state was reached. The macroscopic characteristics, including the shear strength and dilatancy response, were investigated. As E_r increased, the shear strength generally decreased, and the volumetric strain monotonically decreased. Then, the microscopic characteristics, including the coordination number, particle rotation, percentage of sliding contacts and contact force, were examined. Finally, analysis-related anisotropy coefficients of the entire contact network were evaluated to probe the microscopic origins of the peak and residual shear strength related to E_r.

Keywords: Particle shape; Particle erosion; DEM; Triaxial compression;

Macro-micro response; Fabric anisotropy

Introduction

Rocks are affected by various natural factors, such as diurnal and seasonal variations in temperature (Hall et al., 2001), precipitation (Liu et al., 2013), biological action (Charles and Cockell, 2011), and freezing and thawing of water in cracks (Huang et al., 2019), which lead to volume expansion and shrinkage, increase the development of cracks and cause ultimate disintegration into fragments and fine particles. In addition, human activities, such as excavation (Lisjak et al., 2014) and blasting engineering (Ning et al., 2011), can have similar effects on rocks. The fragments and fine particles produced by the aforementioned activities initially exhibit mostly angular shapes. After being subjected to various effects, e.g., climatic change (Caldeira, 2006), scouring and tumbling from running water (Poesen and Lavee, 1994) and the repeated impact and grinding between fragments and particles (Qian et al., 2017; Stachowiak, 1998), the irregular edges and corners gradually disappear due to the stress concentrations at these locations, as characterized by previous studies (Durian et al., 2006; Durian et al., 2007). Moreover, the particle volume gradually decreases as the shape evolves from very angular to well rounded, eventually forming round pebbles. The aforementioned phenomena also exist in various industrial fields, e.g., ballast wear in roadbed engineering and ore dressing and ore handling in mining engineering and rockfill dams. As previous studies (Nouguier-Lehon et al., 2003; Azema and Radjai, 2012; Zhao and Zhou, 2017; Nie et al., 2019; Gong and Liu, 2017; Gong et al., 2019a; Yang and Luo, 2015; Suh et al., 2017; Ng et al., 2018; Emeriault and Claquin, 2004) have reported, the particle shape of granular materials is considered the crucial factor governing their macro-micro mechanical behaviour and physical properties. Because the shapes of fragments or particles change during the erosion process, erosion action inevitably affects the mechanical behaviour of granular materials.

The research objects of previous laboratory experiments and numerical

simulations have systematically investigated the effects of particle shape on the mechanical behaviour of granular materials, e.g., aspect ratio (Gong and Liu, 2017) or elongation (Nouguier-Lehon et al., 2003), platyness (Boton et al., 2013), asphericity (Zhao and Zhou, 2017), angularity (Suh et al., 2017; Azema et al., 2013a), sphericity (Yang and Luo, 2015; Cho et al., 2006), roundness (Nie et al., 2020; Yang and Luo, 2015; Cho et al., 2006) and roughness (Kozicki et al., 2012). However, these studies have rarely focused on the formation history of particle shapes to explore their effects on the mechanical behaviour, especially from the particle erosion perspective. The shapes of the eroded particles seem to be related to the roundness index. However, for angular particles, their erosion mainly occurs near the angular edges and corners. Thus, these particles have unique characteristics inconsistent with roundness (Zhao and Wang, 2016). It is one-sided to consider the effect of particle erosion on mechanical behaviour of granular materials from the perspective of roundness. The shortcomings of the aforementioned studies are the driving force of this work.

To date, many methods have been used to investigate the effect of particle shape on mechanical behaviour, such as laboratory experiments and field tests. Although these experimental tests have acquired ample macroscopic data and provide insights into aspects of particle morphology, there are still many deficiencies of these methods, e.g., large discreteness of results, poor repeatability of processes and insufficient micro-interpretation (Suh et al., 2017; Yagiz, 2001; Chen and Wan, 2004). Numerical simulation, especially the discrete element method (DEM) (Cundall and Strack, 1979) and the contact dynamic method (CDM) , eliminates these limitations and has become an effective tool, allowing the exploration of various types of microscopic mechanical behaviour. In addition, numerical simulations can involve customized geometric models that cannot be easily implemented in physical experiments. Therefore, numerical simulation methods, especially the DEM, have been widely used in research and engineering fields related to particle shape.

In this context, we use a 3D DEM particle system to explore the effect of particle

shape caused by particle erosion on the mechanical behaviour of granular materials. This work is organized as follows. First, the definition of particle erosion degree and the process of assembly formation are briefly introduced. Then, the macroscopic responses, including the shear strength and dilatancy, are presented. Subsequently, microscopic responses, such as the coordination number, particulate rotation, sliding contact and contact force, are investigated. In addition, the fabric anisotropy of the entire contact network is analysed. Finally, the main conclusions of the work are provided.

Definition of erosion degree and DEM modelling

Definition of erosion degree

It is well known that the rounded shapes of pebbles arise because of faster erosion of parts furthest from the centre, which neatly explains why sharp corners are worn away. By laboratory tests, Durian et al. (2006) found that the erosion is fastest at the corners, and once the corners have been removed, the pebble reaches a nearly round shape that progressively shrinks. In this study, it is assumed that the erosion of particles occurs at the edges and corners of particles. Fillets with different radii are constantly used to replace the original edges and corners to simulate the different degrees of particle erosion. In this study, the dimensionless index E_{r} describing erosion degree is defined as follows:

$$E_{\mathrm{r}} = \frac{r}{\sqrt[3]{3V_{\mathrm{ue}}/(4\pi)}} \tag{1}$$

where r is the radius of the rounded corner, as shown in Fig. 1; V_{ue} is the volume of the uneroded particle. In other words, E_{r} indicates the ratio between the radius of the fillet and the radius of the volume-equivalent sphere of the uneroded particle. A schematic diagram for the definition of the degree of particle erosion is illustrated in Fig. 1.

Particle preparation and assembly generation

Numerical simulations were carried out using the DEM program PFC^{3D} (Itasca, 2019). The original uneroded particles used in this study are regular octahedrons.

Generally, greater E_r values correspond to more severe particle erosion, i.e., the edges and corners of eroded particles become much more rounded. The eroded particle geometries are obtained in the modelling package of Rhinoceros and can be converted into a STL-file, which can be directly imported into PFC^{3D} (Itasca, 2019). Here, the STL-file stores a triangular surface mesh used by the rapid prototyping industry as a standard file format. All particles are rigid blocks and without requiring sub-spheres, as shown in Fig. 2. To balance the computational effort and the accuracy of the particle shape, the particles consist of 2100-2600 triangular facets. To generate an eroded particle, the edges of the regular octahedrons are replaced by fillets with a certain radius. This method is generally consistent with the literature (Durian et al., 2006) on the evolution of pebble erosion from square to round. According to Eq. (1), E_r = 0 and 0.8456 represent the particles that were not eroded and entirely eroded into a sphere from a regular octahedron, respectively. Nine types of particles with different E_r are considered, with E_r values of 0.0, 0.1, 0.2, 0.3, 0.4, 0.5, 0.6, 0.7 and 0.8, as shown in Fig. 2. The particle volume decreases with increasing E_r. The volume of a regular octahedron corresponds to the volume of a sphere with a diameter of 2 cm, while E_r=0.8 indicates a sphere with a diameter of 1.73 cm.

Note that the contact type is simplified in PFC6.0 and there is only one contact point for two particles in contact. Namely, different contact types consisting of vertex, edge and face could not be recognized in this study. The simple linear displacement-force contact law (Itasca, 2019), which was used in several previous DEM studies (Gu et al., 2013; Yan, 2009; Yang et al., 2016; Wang et al., 2019), is adopted to model particle-particle and particle-wall interactions. As reported by Zhao et al. (2018), the linear contact model resembles the Hertz-Mindlin model on aspects of both microscopic and macroscopic mechanical behaviour of granular material with spherical and non-spherical particles. The normal contact stiffness k_n of the particles varies according to $k_n = \pi E_c r^2/(r_a + r_b)$, where E_c is the contact effective modulus, r_a and r_b represent the radii of contact, and r is the smaller value of r_a and r_b. After the

k_n value is determined, the shear contact stiffness k_s can be obtained based on $k_s = k_n/k^*$, where k^* is the normal to shear stiffness ratio. The k^* value suggested by Goldenberg and Goldhirsch (2005) for realistic granular materials is in the range of $1.0<k^*<1.5$. Hence, $k^* = 4/3$ was used in this study. All microscale parameters used in the DEM simulation are listed in Table 1.

Particles with random orientations were initially generated within a cube without contact. The cube was modelled using six rigid walls. Taking into account the computational cost, each assembly was limited to 2000 particles. This number is consistent with the similar numbers (1170–3000) used in previous studies (Wang and Gutierrez, 2010; Huang et al., 2014) to explore the mechanical behaviour of granular materials. Temporarily, the acceleration of gravity and the frictional coefficients between particle-particle and particle-wall contacts were set to zero to avoid force gradients and obtain isotropically dense assemblies. The particles were subjected to isotropic compression under a low strain ratio. During isotropic compression, a servo-control mechanism (a built-in function of PFC^{3D}) was introduced to maintain the desired confining pressure ($\sigma_c = 200$kPa). When the stress tolerance was less than 0.5% and the ratio of the average static unbalance force to the average contact force was less than 1×10^{-5}, the assemblies were considered to be equilibrated. Fig. 3 displays several snapshots of the assemblies for several values of E_r at the end of isotropic compaction.

To eliminate the effect of assembly size and minimize stress non-uniformities, Jamiolkowski et al. (2004) suggested that the ratio of the assembly size to the maximum particle size should be greater than 5, with an ideal ratio of 8. In this simulation, this ratio is approximately 12, as shown in Fig. 3. Note that the densest assemblies were produced by setting the friction coefficient to zero during the assembly generation (Abbireddy and Clayton, 2010; Deluzarche and Cambou, 2006). Therefore, all assemblies with different E_r had the same relative density after isotropic compression, as outlined in previous reports (Azema and Radjai, 2012; Rothenburg

and Bathurst, 1992).

After isotropic compression, conventional drained triaxial compression tests were simulated in this study. The isotropic assemblies were subjected to vertical compression by a downward displacement at a constant velocity of the top wall, while the confining pressure σ_c acting on the lateral walls remained constant by the servo-control mechanism. The friction coefficient of particle-particle contacts μ was set to 0.5, while that of wall-particles contact was set to 0.0. To ensure quasi-static shearing, the shear ratio must be sufficiently slow such that kinetic energy generated during shearing is negligible. This can be quantified by an inertia parameter I_m, which is defined as:

$$I_m = \dot{\varepsilon} d \sqrt{\frac{\rho}{p'}} \tag{2}$$

where $\dot{\varepsilon} = v/h_0$ is the shear strain rate, v = 0.15m/s indicates the loading velocity, h_0 denotes the initial assembly height before shear; d is the maximum particle diameter; ρ is the particle density; and p' is the average stress. Perez et al. (2016) recommended that $I_m \leq 2.5\times10^{-3}$. The I_m value is less than 1.5×10^{-3} throughout the simulations.

Macroscopic behaviour

Macroscopic parameters

The macroscale stress tensor for microscale quantities of the contact forces and contact vectors is as follows:

$$\sigma_{ij} = \frac{1}{V}\sum_{c\in N_c} f_i^c l_j^c \tag{3}$$

where V is the volume of the assembly; f_i^c is the ith component of the contact force at contact c within the assembly; l_j^c is the jth component of the contact vector at contact c; and N_c is the total number of contacts. For conventional triaxial stress, the effective mean (p') and deviator (q) can be defined as follows:

$$p' = (\sigma_1 + \sigma_2 + \sigma_3)/3 \tag{4}$$

$$q = \sigma_1 - (\sigma_2 + \sigma_3)/2 \tag{5}$$

where σ_1 is the axial stress and σ_2 and σ_3 represent the lateral stresses. The axial

196 strain ε_1 and the volumetric strain ε_v can be defined as follows:

197 $$\varepsilon_1 = (h_0 - h)/h_0 \quad (6)$$

198 $$\varepsilon_v = (v - v_0)/v_0 \quad (7)$$

199 where h and v are the height and volume of the assembly at a given deformation state,
200 respectively, and h_0 and v_0 are the initial height and volume of the assembly before
201 shear, respectively. Note that a negative value of ε_v represents volume compression
202 in this simulation. The internal friction angle (φ), which represents the shear strength
203 of a granular material, is defined from the stress ratio as follows:

204 $$\sin\varphi = \frac{\sigma_1 - \sigma_3}{\sigma_1 + \sigma_3} = \frac{3q/p'}{q/p' + 6} \quad (8)$$

205 **Shear strength and dilatancy**

206 The purpose of this study is to quantify the effect of particle shape caused by
207 erosion on the mechanical behaviour of granular materials. All assemblies were
208 sheared to an axial strain of ε_1=50%. With such large deformation, typical critical
209 conditions, i.e., a constant stress and a constant volume, are approximately fulfilled.
210 Fig. 4 illustrates the relationship between the initial porosity n_0 and various E_r. The
211 value of n_0 shows an inverse unimodal characteristic, i.e., n_0 first decreases with
212 increasing E_r until it reaches the minimum value at E_r=0.4, and then the trend reverses
213 with a further increase in E_r. Clearly, n_0 can be fitted by the parabolic function of E_r,
214 expressed as n_0= 0.42E_r^2-0.31E_r+0.36.

215 The particle size was slightly decrease with increasing E_r in this study. To
216 investigate the potential effect of the particle size on the stress-strain relationship, four
217 tests were conducted with E_r=0.0 and 0.8 and different particle sizes D. Fig. 5
218 illustrates the stress-strain relationships of these assemblies. It is clear that for a given
219 E_r, the stress-strain curves are generally consistent for different D values, indicating
220 that the particle size has a limited effect on the stress-strain relationships.

221 Fig. 6 shows the stress ratio q/p' versus axial strian ε_1 for all assemblies with
222 various values of E_r. All curves behave in a similar manner as dense cohesion-less
223 granular material. First, q/p' rapidly increases, which reflects both the rigidity of the

particles and the dense packing fraction of the assembly (Azema et al., 2013b). After that, q/p' exceeds the peak value and then gradually decreases to a relatively constant plateau called the critical (residual) state. Obviously, E_r has a great influence on both the peak and the critical shear strengths.

Fig. 7 displays the peak (φ_p) and critical (φ_c) internal friction angles as a function of E_r. Considering the fluctuation in q/p', φ_c is obtained by calculating the mean value of φ_c at the critical state in the interval $\varepsilon_1 \in [35\%, 50\%]$, as shown in Fig. 6. The error bars indicate the deviation of the internal friction angle at the critical state. As shown in Fig. 7, the value of φ_p initially exhibits a high plateau of $\varphi_p \approx 46°$ before E_r=0.2. When E_r > 0.2, the value of φ_p decreases with increasing E_r and approaches the minimum value φ_p=32.2° when E_r = 0.8. The value of φ_p decreases by 14.7° when E_r increases from 0.0 to 0.8. In contrast, the value of φ_c decreases monotonically from 30.7° to 18.5° when E_r increases from 0.0 to 0.8. Correspondingly, the value of φ_c decreases by 12.2°. Azéma et al. (2013) reported that the octahedron assembly has a higher internal friction angle than the sphere assembly; specifically, the values of φ_c for the octahedron and sphere assemblies are 32.1° and 16.6°, respectively. These findings are consistent with the observations in this study.

Fig. 8 exhibits the volumetric strain ε_v versus the axial strain ε_1 for all assemblies with different E_r. The volumetric strain ε_v is initially negative, then gradually increases, and finally converges to a relatively stable state. Thus, the assemblies first exhibit slight compression, then dilatancy and eventually a critical state. This trend is in agreement with the typical response of dense sands observed in the laboratory. The inset displays ε_v at the critical state versus various E_r. Here, ε_v decreases gradually with increasing E_r, indicating that the volume change of assemblies gradually decreases with increasing E_r. This finding is consistent with the previous observations (Zhao et al., 2015) that the angular particles exhibit greater dilatancy than the rounded particles.

Microscopic behaviour

To explore the microscale behaviour at the particle scale, various particle-scale characteristics were investigated, including the coordination number (CN), particle rotation, sliding contact and contact force.

Coordination number

The traditional definition of CN is the average number of particles contacting a particle. Numerically, CN can be calculated as $2N_c/N_p$, where N_c represents the number of contacts within particle system, N_p denotes the number of particles (Markauskas et al., 2010). The CN is an important parameter to quantify the internal structural characteristics of granular materials. Fig. 9 shows the CN value versus ε_1 for all assemblies with various E_r. The value of CN displays a dramatic decline against ε_1 before reaching a low plateau at $\varepsilon_1 \approx 10\%$. A similar trend was described by a theoretical relationship associated with particulate plastic deformation in 2D DEM simulation (Rothenburg and Kruyt, 2004) and particle asphericity using superballs in 3D DEM simulation (Zhao and Zhou, 2017). The CN values at the initial state, peak state and critical state were plotted in the inset. The trends of the CN at the initial and peak states are approximately the same, which remain almost constant when $E_r \leq 0.5$ and then gradually decrease with a further increase in E_r. In addition, the high value of the CN at the initial state is a consequence of isotropic compaction with zero friction. It is interesting that all assemblies exhibit nearly the same plateau of CN ≈ 3.56 at the critical state, nearly independent of E_r. Previous studies (Silbert, 2010) stated that the CN approaches the minimum value required for mechanical stability at the jamming transition, namely, the transition of granular materials from a flow-like to a solid-like state or vice versa. The CN for frictional spheres at the jamming transition is 4.0 for large friction (Zhao et al., 2018), which is slightly larger than that in this study. Indeed, a lower CN of 3.6 at the critical state was observed by Jiang et al. (2015), which is consistent with the finding in this study.

Particle rotation

Rolling and sliding are two important relative movement parameters for each particle in contact. The mean particle rotation within particle system can be obtained as follows:

$$r\_ij\_E_{\mathrm{r}} = \frac{\sum_{m}^{N_{\mathrm{p}}} r_{\mathrm{m}}}{N_{\mathrm{p}}} \tag{9}$$

where r_{m} denotes the rotation around a particular axis of the *m*th particle from the initial state to a specific state; *i* indicates the x, y and z axes; *j* represents *p* and *n*, indicating that the particle rotation is positive or negative around a specific axis, respectively; and E_{r} is the erosion degree. For example, *r_xp*_0.2 indicates that for assembly with E_{r} = 0.2, the mean rotation of particles around the positive *x* axes. Figs. 10(a)-(c) display the evolution of mean particle rotation in the positive and negative directions around three global orthogonal axes (x, y, z) versus the axial strain ε_1, respectively. It is clear that the cumulative rotations are obviously influenced by E_{r}. Generally, at a given strain state, the particle rotation is gradually increased with increasing E_{r}. Namely, when E_{r} increases, the anti-rotation ability of the particles decreases. This finding meets the expectation that the less angular the particle is, the greater rotation of the particle occurs. Note that a similar phenomenon was also observed by Gong and Liu (2017) when studying the effect of the aspect ratio on the shear behaviour of granular materials. Alternatively, because the particle shape of the regular octahedron adopted in this study is isotropic, the cumulative rotations are generally symmetric for a specific axis.

Percentage of sliding contacts

Sliding contact is governed by Coulomb's friction law. The sliding ratio S_{c} can be represented as $S_{\mathrm{c}} = |f_{\mathrm{t}}|/(\mu_{\mathrm{b}} f_{\mathrm{n}})$, where f_{t} and f_{n} are shear and normal forces, respectively, and μ_{b} is the friction coefficient between particles. Sliding contact is considered to occur when $S_{\mathrm{c}} \geq 1.0$. The percentage of sliding contacts SCP can be expressed as SCP = $N_{\mathrm{sc}}/N_{\mathrm{c}} \times 100\%$, where N_{sc} denotes the number of sliding contacts. Fig. 11 shows the evolution of SCP versus the axial strain for all specimens with

different E_r. The SCP initially sharply increases to the peak value at a small axial strain of approximately 1% and then gradually decreases to a relatively stable value, as noted in previous studies (Gong and Liu, 2017; Gu et al., 2013) of dense granular materials. The effect of E_r on the SCP at the stable stage is incorporated. When $E_r \leq$ 0.2, the SCP generally maintains a high plateau and then gradually decreases with an increase in E_r. Estrada et al. (2011) reported that when relative motion occurs between particles in contact, the stronger anti-rotation ability of non-regular particles forces contacts to slide to adjust the overall deformation of the assembly. Therefore, a decrease in the SCP results from the decrease in the anti-rotation ability of particles with increasing E_r, as shown in Fig. 10.

Contact force

The force transmitted during shearing for granular materials is through coexisting strong and weak contacts, which divides the entire contact network into strong and weak subnetworks. To quantitatively investigate the mechanical roles of the two subnetworks, the ξ-network is used to determine the classification indicator proposed by Zhao and Zhou (2017) and Gong et al. (2019c). The ξ-network represents the contact network that the normal contact force is smaller than $\xi\overline{f_n}$, where $\overline{f_n}$ is the mean contact force within the particle system and ξ is in the range of $0 < \xi \leq f_n^{max}/\overline{f_n}$ (f_n^{max} is the maximum normal contact force within particle system). Note that when $\xi = f_n^{max}/\overline{f_n}$, the ξ-network indicates the entire contact network. Fig. 12 represents the relationship between the cumulative $q(\xi)/p'$and ξ at ε_1=50%. Following Radjai et al. (1998), strong and weak subnetworks can be determined by the transition point ξ_c when $q(\xi < \xi_c)/p'$ approaches zero. Previous studies (e.g., Radjai et al. (1998) and Thornton (1998)) have shown that ξ_c= 1.0 can be used to separate strong and weak contacts for spherical particle systems. In addition, the effects of particle shape (Azema and Radjai, 2012; Estrada et al., 2008) and interparticle friction (Gong et al., 2019c) result in the ξ_c value slightly deviating

from 1.0. In this study, the $q(\xi < 1.0)/p'$ remains a relatively low value (< 0.1) for all assemblies, as shown in Fig. 12. Therefore, ξ_c=1.0 is regarded as a general index to separate strong and weak contacts.

External loads of a particle system transmit through the contacts between particles, which form the contact force networks that have been regarded as an important factor affecting the mechanical behaviour of granular systems (Radjai et al., 1998). Fig. 13 shows maps of the normal contact force of the assembly with E_r = 0.4 at three states (i.e., the initial, peak and critical states). The line in Fig. 13 links the centres of particles in contact, and the thickness is proportional to the magnitude of the normal contact force. At the initial state (see Fig. 13(a)), the normal contact forces are isotropic within an assembly because the assembly has been subjected to isotropic compression. At the peak state (see Fig. 13(b)), the normal contact forces close to the vertical direction are clearly greater, showing obvious anisotropy. Although the strong contact forces are sparse, they are sufficient to bear the external loading as pillars. In addition, the weak contact forces play an indispensable role in contributing to the stability of strong contact forces (Radjai et al., 1998). At the critical state (see Fig. 13(c)), the strong normal contact forces become sparser than in the peak state and show obvious anisotropy.

Fig. 14 shows the mean normal and mean shear contact forces versus E_r at the critical state. Both the normal and shear contact forces decrease nearly linearly with increasing E_r. In addition, the ratio of the normal contact force to the shear contact force gradually decreases with increasing E_r, as shown in the figure. This phenomenon leads to decreased sliding contacts, as observed in the inset in Fig. 11.

Fabric anisotropy and origins of shear strength

The macroscopic and microscopic characteristics described above indicate the effects of E_r on mechanical behaviour for granular materials. To investigate the relationship between macroscopic and microscopic characteristics, fabric anisotropy is introduced in this section. Emphasis is placed on exploring the effect of E_r on fabric

anisotropy as well as the relationship between fabric anisotropy and shear strength.

The relationship between the stress-force-fabric relationship (SFF for short) and the stress ratio were derived by Ouadfel and Rothenburg (2001) in 3D domains as follows:

$$q/p' = 0.4(a_c + a_n + 1.5a_t + a_{dn} + 1.5a_{dt}) \quad (10)$$

In 2D domains, the relationship in Eq. 10 can be written as $q/p' = 0.5(a_c + a_n + a_t + a_{dn} + a_{dt})$ as derived by Rothenburg and Bathurst (1989). Here, a_c, a_n, a_t, a_{dn} and a_{dt} are the anisotropic coefficients and reflect the degree of normal contact anisotropy, normal contact force anisotropy, shear contact force anisotropy, normal branch vector anisotropy and shear branch vector anisotropy, respectively. To validate the SFF relationship, the stress ratio q/p' derived from the walls is compared with that obtained from sources of anisotropy (Fig. 15). Fig. 15(a) displays the contribution of each anisotropy component to the shear strength for the assembly with E_r = 0.0. Fig. 15(b) illustrates the evolution in q/p' determined using Eq. (10) at the peak and critical states, with varying E_r. In Figs. 15(a)-(b), it is clear that q/p' obtained from the walls agrees well with that derived from Eq. (10), albeit with slight deviations. These deviations are attributed mainly to omission of the cross product of the anisotropy tensor in Eq. (10). Fig. 15 denotes that the fabric anisotropies of granular materials are the essential origin of their shear strengths, which can help us understand the distinctive effects of different anisotropy sources on the shear strengths. For example, as observed in Fig. 15(a), $0.4a_n$ underpins the shear strength, which is consistent with the results presented by Guo and Zhao (2013) and Gu et al. (2013). Alternatively, $0.4a_c$ and $0.6a_t$ make secondary and tertiary contributions to the shear strength, respectively, and the contributions of $0.4a_{dn}$ and $0.6a_{dt}$ are very small and can be neglected.

The variations in these anisotropic coefficients at both peak and critical states with respect to E_r are illustrated in Figs. 16(a)-(b). It can be observed that $1.5a_{dt}$ and a_{dn} remain nearly unchanged at both peak and critical states, and their contributions

are considered negligible. Alternatively, with the evolutions of a_c, a_n and a_t, the peak and critical states are generally consistent. Specifically, at the peak state, as shown in Fig. 16(a), the variations in a_c, a_n and a_t only slightly decrease with increasing E_r when $E_r < 0.5$. However, the values of a_c, a_n and a_t show a more rapid decrease when $E_r \geq 0.5$. At the critical state, as shown in Fig. 16(b), both a_c and a_t exhibit a decreasing trend with increasing E_r. Regarding the evolution of a_n, this parameter remains nearly unchanged when $E_r < 0.2$ and then gradually decreases with increasing E_r when $E_r \geq 0.2$. Generally, the observations indicate that the contact anisotropy and normal and shear contact force anisotropies decrease with increasing particle erosion degree. This finding can also be reflected by the rose diagrams of the contact number, normal contact force (CNF) and shear contact force (CSF) at the critical state, as shown in Fig. 17. The SFF relationship enables us to understand the microscopic mechanism of the macroscopic shear strengths. That is, the decreased peak and critical shear strengths are attributed mainly to the decreases in a_c, a_n and a_t, while the contributions of a_{dn} and a_{dt} can be neglected.

As reported by several previous researchers (Gong et al., 2019b; Sufian et al., 2017), the anisotropy within a strong and non-sliding contact a_c^{sn} exhibits a linear relationship with the stress ratio q/p' (i.e., $q/p' = k a_c^{sn}$). Note that k is the fit coefficient and has no explicit physical meaning; the a_c^{sn} indicate the normal contact anisotropy restriction to strong and non-sliding contact. Previous DEM studies (i.e., Gong et al. 2019b, Gong et al. 2019c) have reported that the k value is influenced by the particle shape and friction between particles. Fig. 18 illustrates the relationships between q/p' and a_c^{sn} for various assemblies. The solid lines represent the linear fittings for these relationships. It is clear that the fitting lines pass through the origin, and the high values of $R^2 \in (0.96, 0.98)$ indicate that the relationships between q/p' and a_c^{sn} are nearly linear for various E_r. The variations in a_c^{sn} at the critical state and the fit coefficient (i.e., k) with E_r are plotted in the inset. Here, a_c^{sn} gradually decreases with increasing E_r. Alternatively, k first remains nearly unchanged when E_r

417 < 0.6, despite some fluctuations. Then, k gradually decreases with increasing E_r when
418 $E_r \geq 0.6$. Based on $q/p' = ka_c^{sn}$, the evolution of φ_c can be understood. Specifically,
419 a decrease in φ_c is related to both decrease in k and a_c^{sn}.

420 ## Conclusion

421 In this paper, the effect of particle shape caused by erosion on macroscopic and
422 microscopic mechanical behaviour under quasi-static shearing is quantitatively
423 analysed using rigid blocks via the 3D DEM. The degree of particle erosion was
424 defined using the index E_r, i.e., the ratio of the rounded corner size to the radius of the
425 sphere whose volume is equal to the uneroded particle. Assemblies with eight
426 different E_r values (i.e., 0.0, 0.1, 0.2, 0.3, 0.4, 0.5, 0.6, 0.7, 0.8 and 0.9) were created.
427 Each assembly was composed of 2000 particles. Conventional triaxial compression
428 tests were conducted. The macroscopic and microscopic mechanical behaviours were
429 obtained from our numerical simulation. The main conclusions are summarized as
430 follows.

431 Referring to the macroscopic behaviours, the shear strength at the peak and
432 critical states decreases with increasing E_r. In addition, the assemblies show less
433 dilatancy with increasing E_r. Referring to the microscopic behaviour, it is found that
434 the CN at the critical state remains a constant (≈ 3.56) for different E_r. The rotation
435 increases with E_r due to the decrease in the anti-rotation ability, which also results in a
436 decrease in the percentage of sliding contacts. Fabric anisotropy analyses elucidate the
437 essential origins of the shear strength. For the entire contact network, the normal
438 contact force anisotropy a_n underpins the shear strength, while the normal contact
439 anisotropy a_c and shear contact force anisotropy a_t generally make secondary and
440 tertiary contributions to the shear strength, respectively, and the contributions of
441 normal (a_{dn}) and shear (a_{dt}) branch vector anisotropy can be neglected. With
442 increasing E_r, the shear strength at the peak and critical states decreases due to the
443 decreases in a_c, a_n, and a_t, ignoring changes in a_{dn} and a_{dt}. The SFF relationship
444 enables us to understand the microscopic mechanism of the macroscopic shear

strengths. That is, the decreased peak and critical shear strengths are attributed mainly to the decreases in a_c, a_n and a_t. Furthermore, the relationships between q/p' and a_c^{sn} are nearly linear (i.e., $q/p' = ka_c^{sn}$) for different E_r. Accordingly, the φ_c evolution can also be understood as follows. The decrease in φ_c is related to the both decrease in k and a_c^{sn}.

Acknowledgments

The authors appreciate the constructive comments and suggestions offered by the two anonymous reviewers, Prof Xiaoqiang Gu of TJU, Dr Ning Guo of ZJU and Dr Shiwei Zhao of HKUST on the manuscript. This research was financially supported by National Natural Science Foundation of China (by Project No. 51809292, 51878668), the Innovation-Driven Project of Central South University (Grant No. 2019CX011). The authors would like to express their appreciation for the financial assistance.

References

Abbireddy, C.O.R.,Clayton, C.R.I., 2010. Varying initial void ratios for DEM simulations. Geotechnique. 60 (6), 497-502.

Azéma, E.,Radjai, F., 2012. Force chains and contact network topology in sheared packings of elongated particles. Phys Rev E Stat Nonlin Soft Matter Phys. 85 (3 Pt 1), 031303.

Azéma, E., Estrada, N.,Radjai, F., Shear strength, force distributions and friction mobilization in sheared packings composed of angular particles, AIP Conference Proceedings, 2013, pp. 511-514.

Azéma, E., Radjai, F.,Dubois, F., 2013. Packings of irregular polyhedral particles: strength, structure, and effects of angularity. Phys Rev E Stat Nonlin Soft Matter Phys. 87 (6), 062203.

Boton, M., Azéma, E., Estrada, N., Radjaï, F.,Lizcano, A., 2013. Quasistatic rheology and microstructural description of sheared granular materials composed of platy particles. Phys Rev E. 87 (3).

473 Caldeira, K., 2006. Forests, climate, and silicate rock weathering. J. Geochem Explor.
474 88 (1-3), 419-422.
475 Charles, S.,Cockell, 2011. Biological Volcanic Rock Weathering. Encyclopedia of
476 Geobiology. 143-147.
477 Chen, H.,Wan, J.-P., 2004. The effect of orientation and shape distribution of gravel
478 on slope angles in central Taiwan. Eng Geol. 72 (1-2), 19-31.
479 Cho, G.-C., Dodds, J.,Santamarina, J.C., 2006. Particle Shape Effects on Packing
480 Density, Stiffness, and Strength: Natural and Crushed Sands. J. Geotech
481 Geoenviron. 132 (5), 591-602.
482 Cundall, P.A.,Strack, O.D.L., 1979. A distinct element model forgranular assemblies.
483 Geotechnique. 29 (1), 47-65.
484 Deluzarche, R.,Cambou, B., 2006. Discrete numerical modelling of rockfill dams. Int.
485 J. Numer Anal Met. 30 (11), 1075-1096.
486 Durian, D.J., Bideaud, H., Duringer, P., Schr¨oder, A., Thalmann, F.,Marques, C.M.,
487 2006. What is in a pebble shape? Phys Rev Lett. 97 (5), 028001.
488 Durian, D.J., Bideaud, H., Duringer, P., Schroder, A.P.,Marques, C.M., 2007. Shape
489 and erosion of pebbles. Phys Rev E Stat Nonlin Soft Matter Phys. 75 (2 Pt 1),
490 021301.
491 Emeriault, F.,Claquin, C., 2004. Statistical homogenization for assemblies of elliptical
492 grains: effect of the aspect ratio and particle orientation. Int. J. Solids Struct. 41
493 (21), 5837-5849.
494 Estrada, N., Azéma, E., Radjaï, F.,Taboada, A., 2011. Identification of rolling
495 resistance as a shape parameter in sheared granular media. Phys Rev E 84(1 Pt
496 1):011306.
497 Estrada, N., Taboada, A.,Radjai, F., 2008. Shear strength and force transmission in
498 granular media with rolling resistance. Phys Rev E. 78(1): 021301.
499 Goldenberg, C.,Goldhirsch, I., 2005. Friction enhances elasticity in granular solids.
500 Nature. 435 (7039), 188–191.

Gong, J.,Liu, J., 2017. Effect of aspect ratio on triaxial compression of multi-sphere ellipsoid assemblies simulated using a discrete element method. Particuology. 32, 49-62.

Gong, J., Liu, J.,Cui, L., 2019a. Exploring the effects of particle shape and content of fines on the shear behavior of sand-fines mixtures via the DEM. Comput Geotech. 106, 161-176.

Gong, J., Liu, J.,Cui, L., 2019b. Shear behaviors of granular mixtures of gravel-shaped coarse and spherical fine particles investigated via discrete element method. Powder Technol. 353, 178-194.

Gong, J., Zou, J., Zhao, L., Li, L.,Nie, Z., 2019c. New insights into the effect of interparticle friction on the critical state friction angle of granular materials. Comput Geotech. 113.

Gu, X., Huang, M.,Qian, J., 2013. DEM investigation on the evolution of microstructure in granular soils under shearing. Granul Matter. 16 (1), 91-106.

Guo, N.,Zhao, J., 2013. The signature of shear-induced anisotropy in granular media. Comput Geotech. 47, 1-15.

Hall, K., Marie-Francoise,Andre, 2001. New insights into rock weathering from high-frequency rock temperature data: an Antarctic study of weathering by thermal stress. Geomorphology. 41 (1), 23-25.

Huang, S., Liua, Y., Guoa, Y., Zhanga, Z.,Cai, Y., 2019. Strength and failure characteristics of rock-like material containing single crack under freeze-thaw and uniaxial compression. Cold Reg Sci Technol. 162, 1-10.

Huang, X., Hanley, K.J., O'Sullivan, C.,Kwok, F.C.Y., 2014. Effect of sample size on the response of DEM samples with a realistic grading. Particuology. 15, 107-115.

Itasca, 2019. User's manual for pfc3d. Minneapolis, USA, Itasca Consulting Group, Inc.

Jamiolkowski, M., Kongsukprasert, L.,Presti, D.L., 2004. Characterization of gravelly geomaterials. In Proceedings of the fifth international geotechnical

conference(November).

Jiang, M., Shen, Z.,Wang, J., 2015. A novel three-dimensional contact model for granulates incorporating rolling and twisting resistances. Comput Geotech. 65, 147-163.

Kozicki, J., Tejchman, J.,Mróz, Z., 2012. Effect of grain roughness on strength, volume changes, elastic and dissipated energies during quasi-static homogeneous triaxial compression using DEM. Granul Matter. 14 (4), 457-468.

Lisjak, A., Figi, D.,Grasselli, G., 2014. Fracture development around deep underground excavations: Insights from FDEM modelling. J. Rock Mech Geotech Eng. 6, 493-505.

Liu, T., Cao, P.,Lin, H., 2013. Evolution Procedure of Multiple Rock Cracks under Seepage Pressure. Math Probl Eng. 2013, 1-11.

Markauskas, D., Kačianauskas, R., Džiugys, A.,Navakas, R., 2010. Investigation of adequacy of multi-sphere approximation of elliptical particles for DEM simulations. Granul Matter. 12 (1), 107-123.

Ng, T.-T., Zhou, W., Ma, G.,Chang, X.-L., 2018. Macroscopic and microscopic behaviors of binary mixtures of different particle shapes and particle sizes. Int. J. Solids Struct. 135, 74-84.

Nie, Z., Zhu, Y., Wang, X.,Gong, J., 2019. Investigating the effects of Fourier-based particle shape on the shear behaviors of rockfill material via DEM. Granul Matter. 21 (2).

Nie, Z., Fang, C., Gong, J.,Liang, Z., 2020. DEM study on the effect of roundness on the shear behaviour of granular material. Comput Geotech. 121.

Ning, Y., Yang, J., An, X.,Ma, G., 2011. Modelling rock fracturing and blast-induced rock mass failure via advanced discretisation within the discontinuous deformation analysis framework. Comput Geotech. 38, 40-49.

Nouguier-Lehon, C., Cambou, B.,Vincens, E., 2003. Influence of particle shape and angularity on the behaviour of granular materials: a numerical analysis. Int. J.

557 Numer Anal Met. 27 (14), 1207-1226.
558 Ouadfel, H.,Rothenburg, L., 2001. `Stress-force-fabric' relationship for assemblies of
559 ellipsoids. Mech Mater. 33 (4), 20-221.
560 Perez, J., Kwok, C., O'Sullivan, C., Huang, X.,Hanley, K., 2016. Assessing the
561 quasi-static conditions for shearing in granular media within the critical state soil
562 mechanics framework. Soils Found. 56 (1), 152-159.
563 Poesen, J.,Lavee, H.J., 1994. Rock fragments in top soils: significance and processes.
564 Catena. 23 (1-2), 1-28.
565 Qian, Y., Boler, H., Moaveni, M., Tutumluer, E., Hashash, Y.M.A.,Ghaboussi, J., 2017.
566 Degradation-Related Changes in Ballast Gradation and Aggregate Particle
567 Morphology. J. Geotech GeoenvirO. 143 (8).
568 Radjai, F., E, W.D., Jean.Michel,Moreau.Jean-Jacques, 1998. Bimodal Character of
569 Stress Transmission in Granular Packings. Phys Rev Lett. 80 (1), 61-64.
570 Rothenburg, L.,Bathurst, R.J., 1989. Analytical study of induced anisotropy
571 inidealized granular materials. Geotechnique. 39 (4), 601-614.
572 Rothenburg, L.,Bathurst, R.J., 1992. Micromechanical features of granular assemblies
573 with planar elliptic particles. Geotechnique. 42 (1), 79-95.
574 Rothenburg, L.,Kruyt, N.P., 2004. Critical state and evolution of coordination number
575 in simulated granular materials. Int. J. Solids Struct. 41 (21), 5763-5774.
576 Silbert, L.E., 2010. Jamming of frictional spheres and random loose packing. Soft
577 Matter. 6 (13).
578 Stachowiak, G.W., 1998. Numerical characterization of wear particles morphology
579 and angularity of particles and surfaces. Tribol Inter. 31, 139-157.
580 Sufian, A., Russell, A.R.,Whittle, A.J., 2017. Anisotropy of contact networks in
581 granularmedia and its influence on mobilised internal friction. Geotechnique. 67
582 (12), 1067-1080.
583 Suh, H.S., Kim, K.Y., Lee, J.,Yun, T.S., 2017. Quantification of bulk form and
584 angularity of particle with correlation of shear strength and packing density in

585 sands. Eng Geol. 220, 256-265.
586 Thornton, C., 1998. Quasi-static shear deformation of particulate media. Phil. Trans.
587 R. Soc. Lond. A. 356 (1747), 2763-2782.
588 Wang, J.,Gutierrez, M., 2010. Discrete element simulations of direct shear specimen
589 scale effects. Geotechnique. 60 (5), 395-409.
590 Wang, R., Dafalias, Y.F., Fu, P.,Zhang, J.-M., 2019. Fabric evolution and dilatancy
591 within anisotropic critical state theory guided and validated by DEM. Int. J. Solids
592 Struct.
593 Yagiz, S., 2001. Brief note on the influence of shape and percentage of gravel on the
594 shear strength of sand and gravel mixtures. B Eng Geol Environ. 60 (4), 321-323.
595 Yan, W.M., 2009. Fabric evolution in a numerical direct shear test. Comput Geotech.
596 36 (4), 597-603.
597 Yang, J.,Luo, X.D., 2015. Exploring the relationship between critical state and particle
598 shape for granular materials. J. Mech Phys Solids. 84, 196-213.
599 Yang, Y., Wang, J.F.,Cheng, Y.M., 2016. Quantified evaluation of particle shape
600 effects from micro-to-macro scales for non-convex grains. Particuology. 25, 23-35.
601 Zhao, B.,Wang, J., 2016. 3D quantitative shape analysis on form, roundness, and
602 compactness with μCT. Powder Technol. 291, 262-275.
603 Zhao, S., Evans, T.,Zhou, X., 2018. Effects of curvature-related DEM contact model
604 on the macro-and micro-mechanical behaviours of granular soils. Geotechnique. 17
605 (158), 21.
606 Zhao, S., Evans, T.M.,Zhou, X., 2018. Shear-induced anisotropy of granular materials
607 with rolling resistance and particle shape effects. Int. J. Solids Struct. 150, 268-281.
608 Zhao, S., Zhou, X.,Liu, W., 2015. Discrete element simulations of direct shear tests
609 with particle angularity effect. Granul Matter. 17 (6), 793-806.
610 Zhao, S.,Zhou, X., 2017. Effects of particle asphericity on the macro- and
611 micro-mechanical behaviors of granular assemblies. Granul Matter. 19 (2).

Table(s)

One table in this study

Table 1. Microscale parameters used in the DEM simulation

Parameter	Value
Particle density (kg/m^3)	2600
Interparticle frictional coefficient	0.5
Wall-particle frictional coefficient	0.0
Normal stiffness of wall-particle contacts (N/m)	1×10^9
Effective modulus, E_c (Pa)	1×10^8
Stiffness ratio (k_n/k_s)	4/3
Damping factor	0.7

Figure(s)

Eighteen figures in this study

Fig. 1. Schematic diagram for the definition of particle erosion degree E_r.

Fig. 2. The left side shows particles with different E_r. From left to right, from top to bottom, particles have E_r values of 0.0, 0.1, 0.2, 0.3, 0.4, 0.5, 0.6, 0.7 and 0.8. The right side displays a particle with E_r=0.5 composed of 2100 triangular facets.

Fig. 3. Snapshot of the assemblies at the end of isotropic compression with (a) E_r = 0.0, (b) E_r= 0.4 and (c) E_r= 0.8.

Fig. 4. Initial porosities for all assemblies with various E_r.

Fig. 5. Evolutions of the stress ratio with axial strain for assemblies with different E_r and volumes. S1 and S2 represent the particles with E_r=0.0 and 0.8, respectively.

Fig. 6. The stress ratio-axial strain responses for assemblies with different E_r.

Fig. 7. Variations in the friction angles at the peak and critical states with respect to E_r; red error bars represent the standard deviation in the critical state.

Fig. 8. Volumetric strain ε_v versus axial strain ε_1 for all assemblies with various E_r. The inset exhibits the relationship between the critical ε_v and E_r at the critical state. The error bars indicate the standard deviation of the strain fluctuations at the critical state.

Fig. 9. Evolution of the mean coordination number CN versus axial strain ε_1 for all assemblies with various E_r. The inset shows the value of the CN versus various E_r at the initial, peak and critical states.

Fig. 10. The particle rotation versus axial strain, (a) x-axis; (b) y-axis; (c) z-axis. Note that positive and negative values represent counter clockwise and clockwise rotation around a particular axis, respectively.

Fig. 11. The percentage of sliding contacts SCP versus the axial strain. The inset shows the relationship between the SCP at the stable state and E_r. Error bars represent the standard deviation at the stable state.

Fig. 12. Cumulative stress ratio $q(\xi)/p'$ as a function of ξ at ε_1=50% for different E_r.

Fig. 13. Maps of normal contact force at initial (a), peak (b) and critical (c) states for the assembly with E_r=0.4. The line thickness is proportional to the magnitude of the normal contact force.

Fig. 14. Mean normal and shear contact forces at the critical state; error bars display the deviation of contact forces at the critical state. The inset shows the ratio of f_s to μf_n.

Fig. 15. Validating the SFF relationship: (a) evolution of the effective stress ratio q/p' and anisotropies with axial strain for E_r=0.0 and (b) evolution of q/p' at the peak and critical states with different roundness along with the analytical expression given in Eq. (21); error bars denote the standard deviation at the critical state.

Fig. 16. Variation in anisotropic coefficients (i.e., a_c, a_n, $1.5a_t$, a_{dn} and $1.5a_{dt}$) with varying E_r at the (a) peak state and (b) critical state.

Fig. 17. Rose diagrams of (a) the contact number, (b) contact normal force (CNF) and (c) contact shear force (CSF) for all assemblies at the critical state. From left to right, rose diagrams represent the evolution of E_r from 0.0 to 0.8.

Fig. 18. Linear relationship between the macroscopic stress ratio and the anisotropy within a strong and non-sliding contact a_c^{sn}. The inset illustrates the evolutions of k and a_c^{sn} at the critical state with E_r.

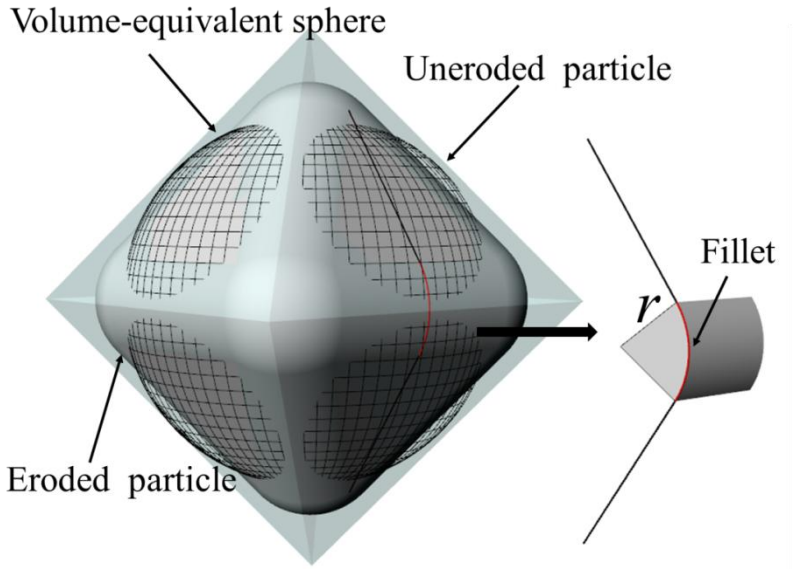

Fig. 1. Schematic diagram for the definition of particle erosion degree E_r.

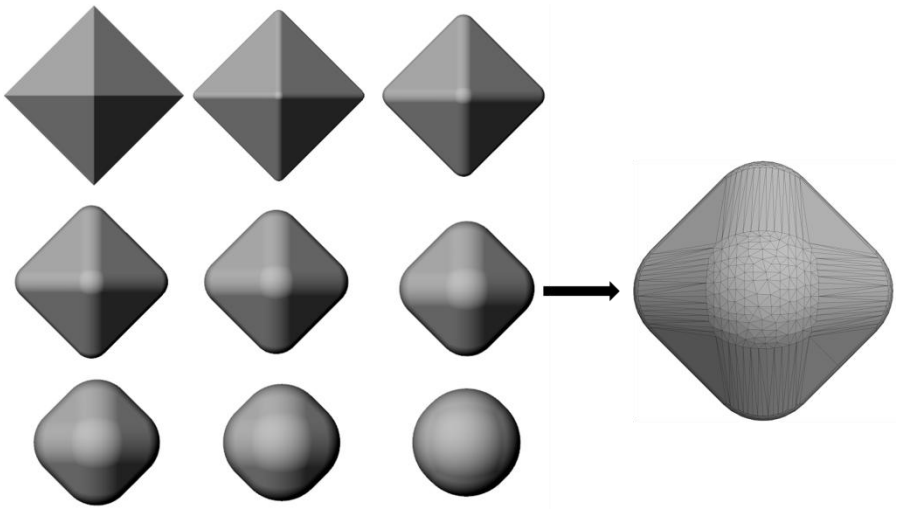

Fig. 2. The left side shows particles with different E_r. From left to right, from top to bottom, particles have E_r values of 0.0, 0.1, 0.2, 0.3, 0.4, 0.5, 0.6, 0.7 and 0.8. The right side displays a particle with E_r=0.5 composed of 2100 triangular facets.

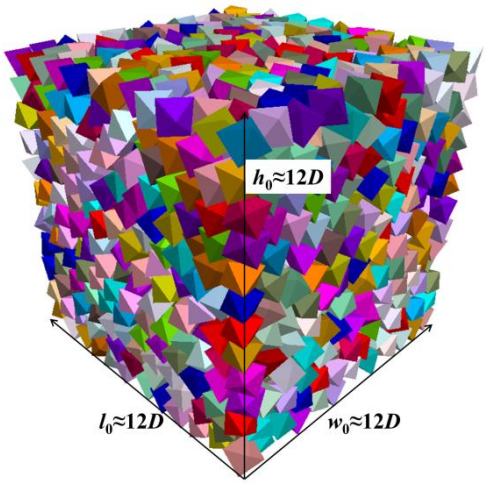

(a)

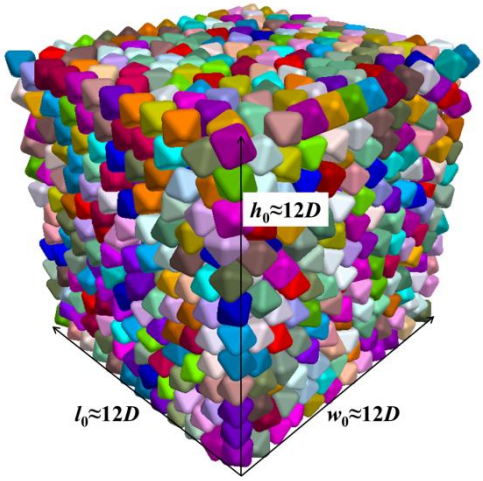

(b)

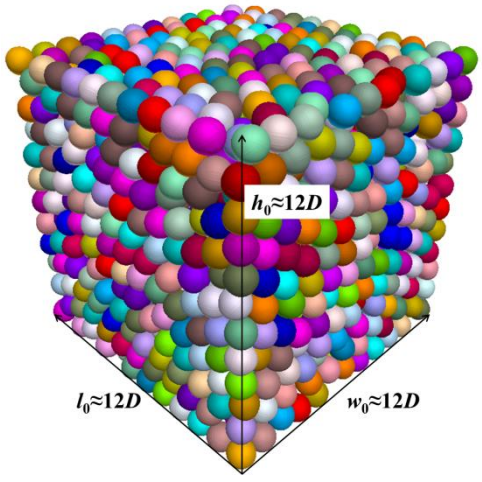

(c)

Fig. 3. Snapshots of the assemblies at the end of isotropic compression with (a) E_r = 0.0, (b) E_r= 0.4 and (c) E_r= 0.8.

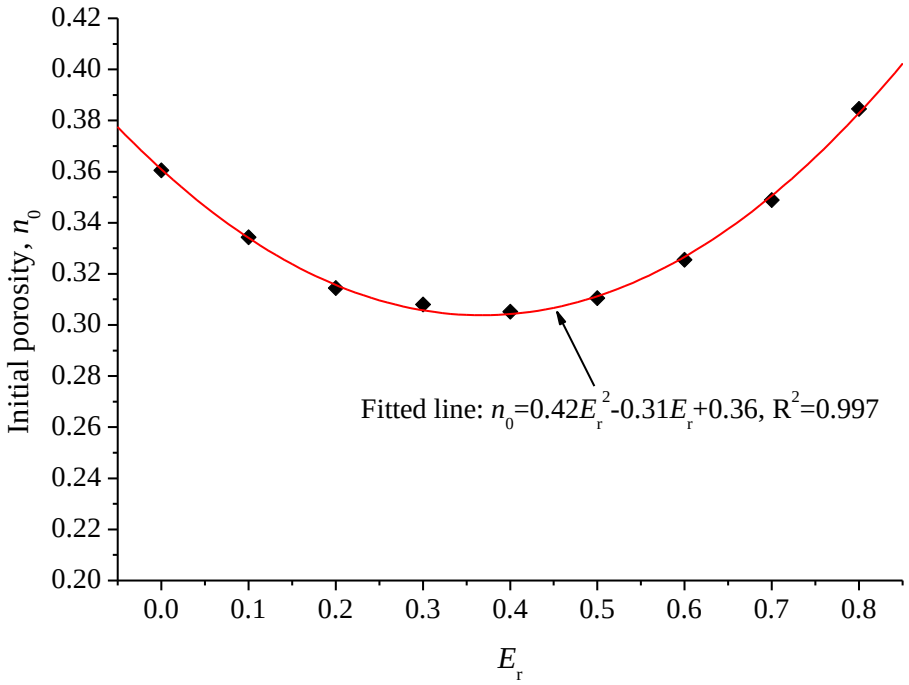

Fig. 4. Initial porosities for all assemblies with various E_r.

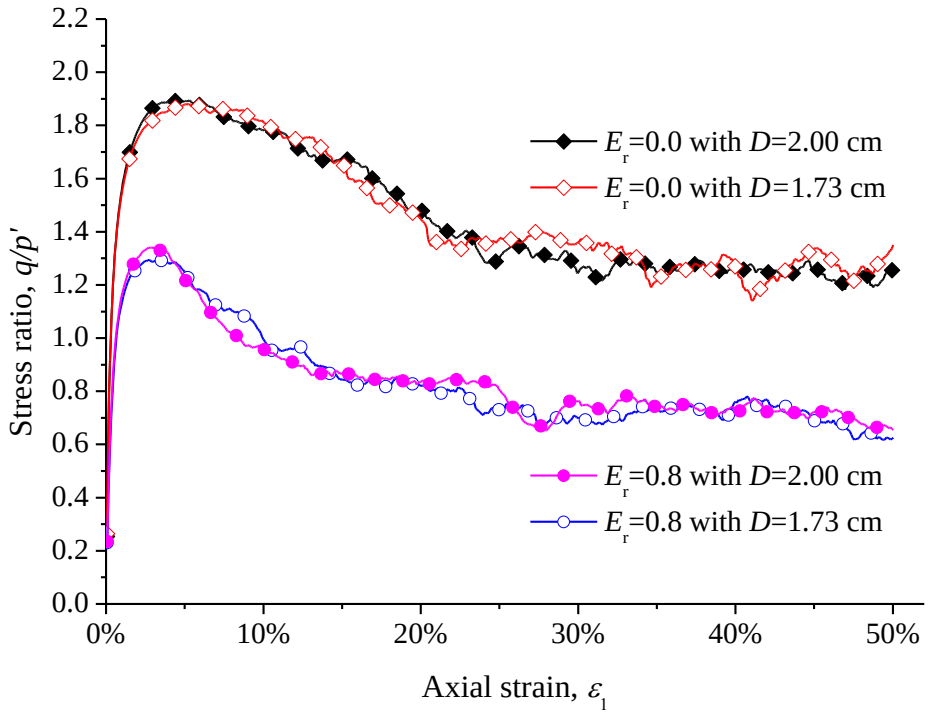

Fig. 5. Evolutions of the stress ratio with axial strain for assemblies with different E_r and volumes. D is the diameter of a reference spherical particle having the same volume as the particles.

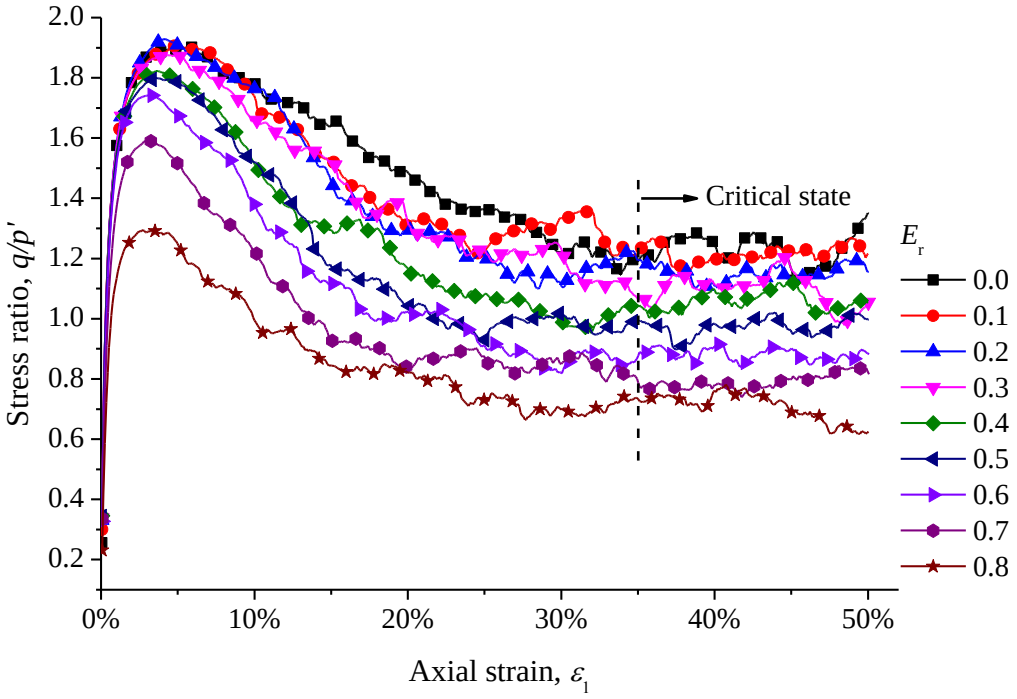

Fig. 6. The stress ratio-axial strain responses for assemblies with different E_r.

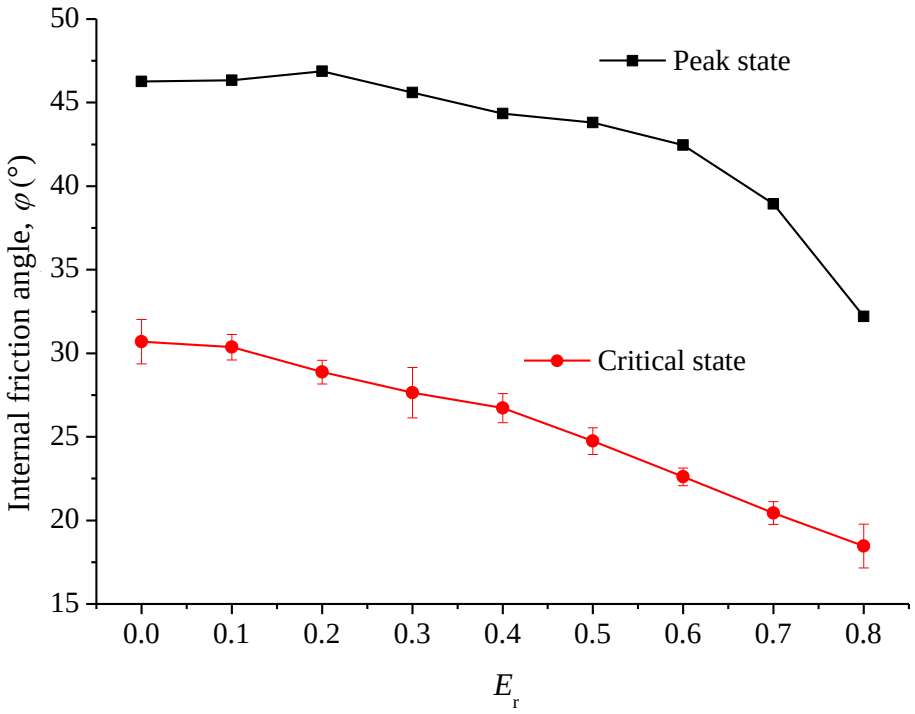

Fig. 7. Variations in the friction angles at the peak and critical states with respect to E_r; red error bars represent the standard deviation in the critical state.

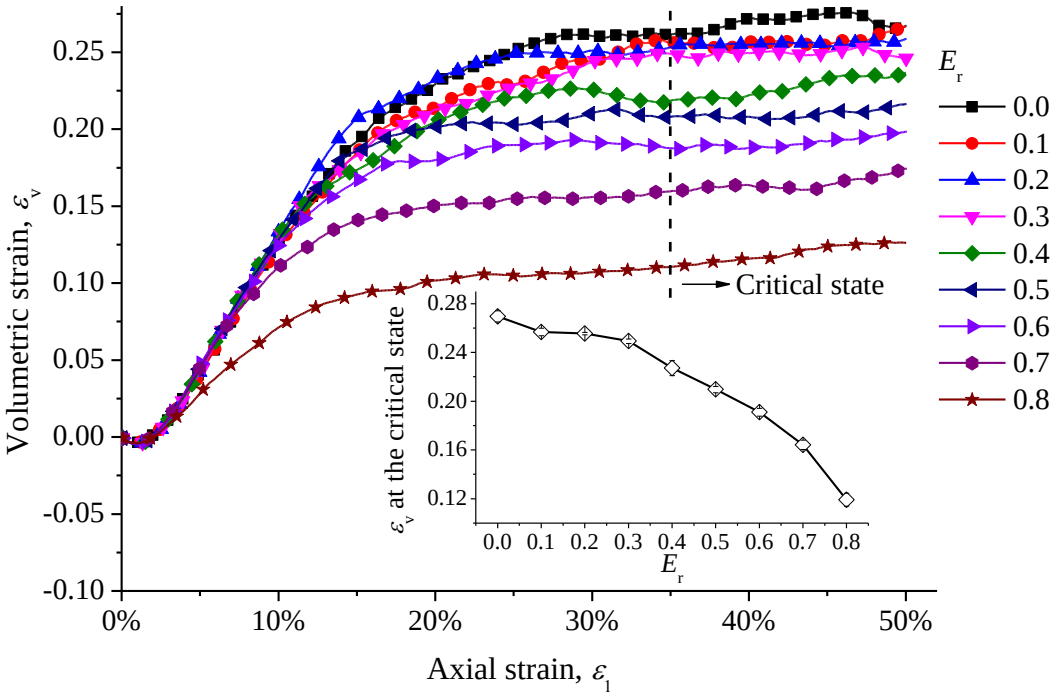

Fig. 8. Volumetric strain ε_v versus axial strain ε_1 for all assemblies with various E_r. The inset exhibits the relationship between the critical ε_v and E_r at the critical state. The error bars indicate the standard deviation of the strain fluctuations at the critical state.

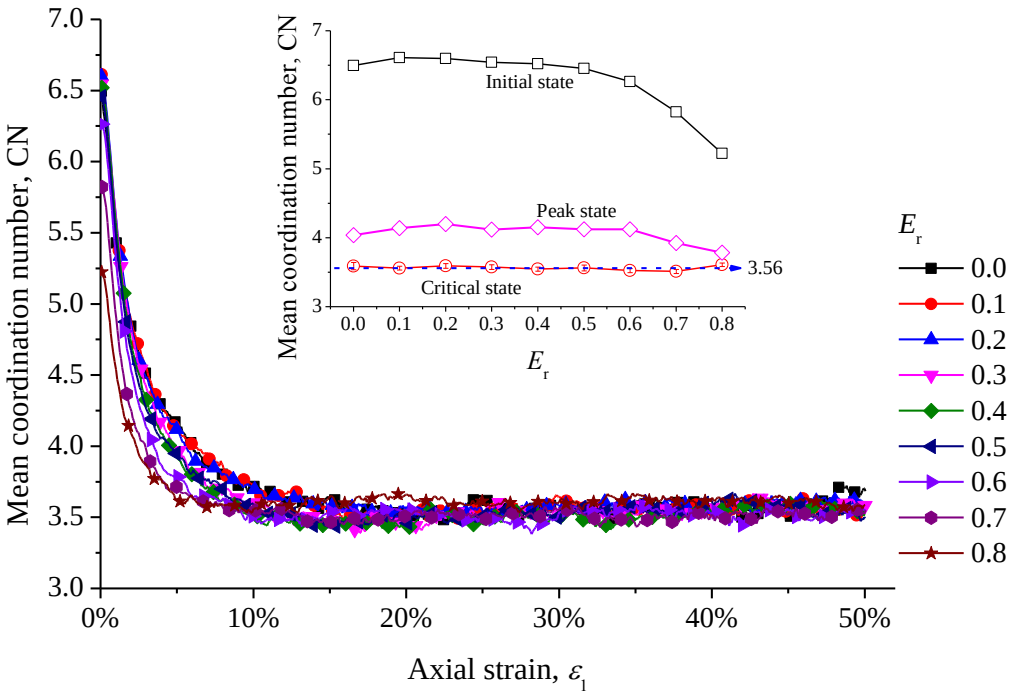

Fig. 9. Evolution of the mean coordination number CN versus axial strain ε_1 for all assemblies with various E_r. The inset shows the value of the CN versus various E_r at the initial, peak and critical states.

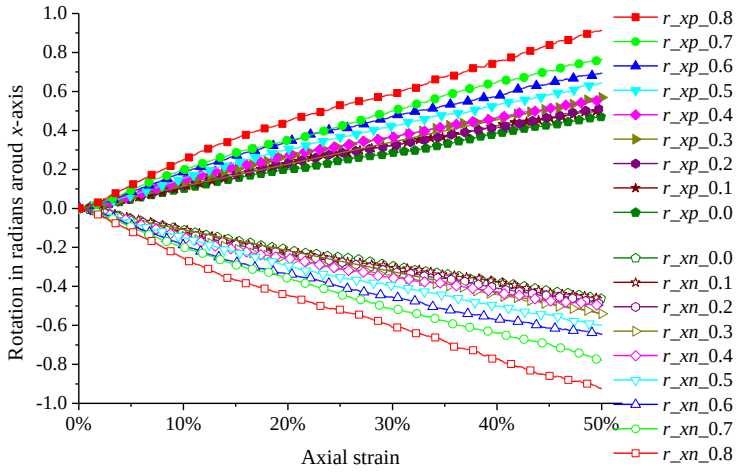

(a)

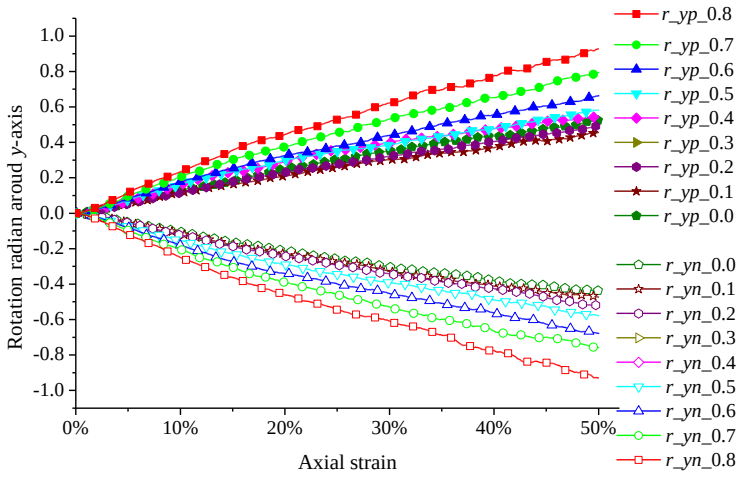

(b)

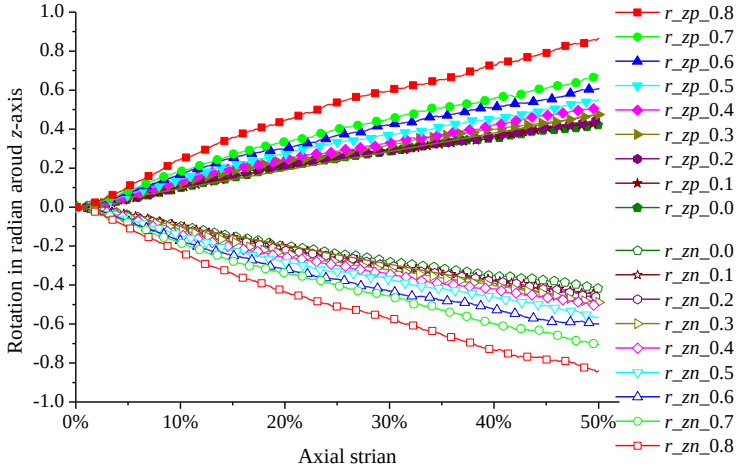

(c)

Fig. 10. The particle rotation versus axial strain, (a) x-axis; (b) y-axis; (c) z-axis. Note that positive and negative values represent counter clockwise and clockwise rotation around a particular axis, respectively.

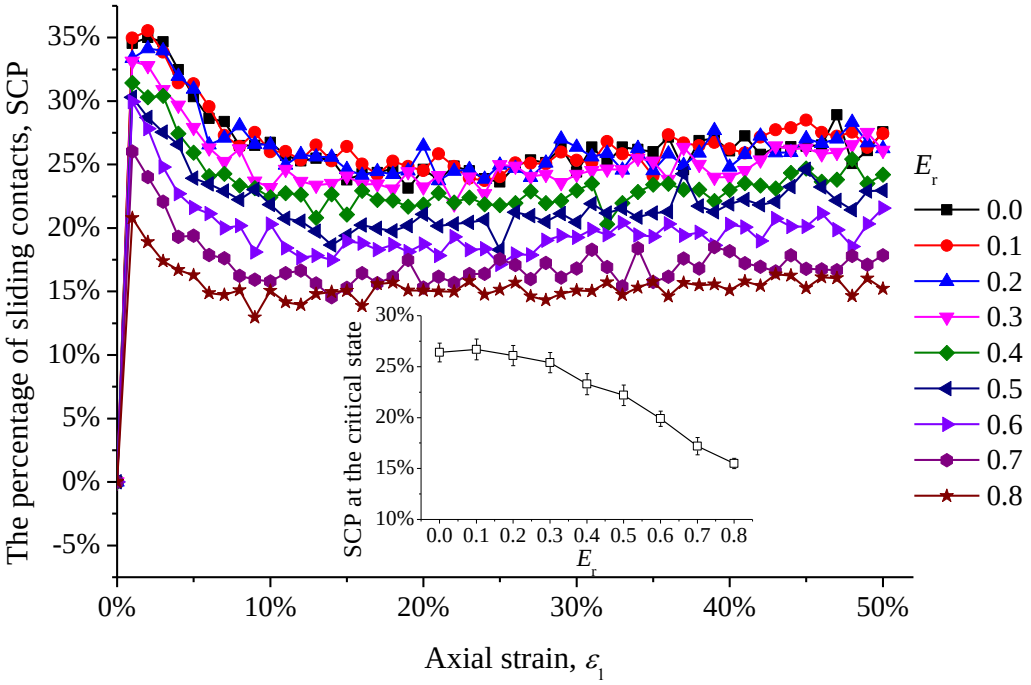

Fig. 11. The percentage of sliding contacts SCP versus the axial strain. The inset shows the relationship between the SCP at the stable state and E_r. Error bars represent the standard deviation at the stable state.

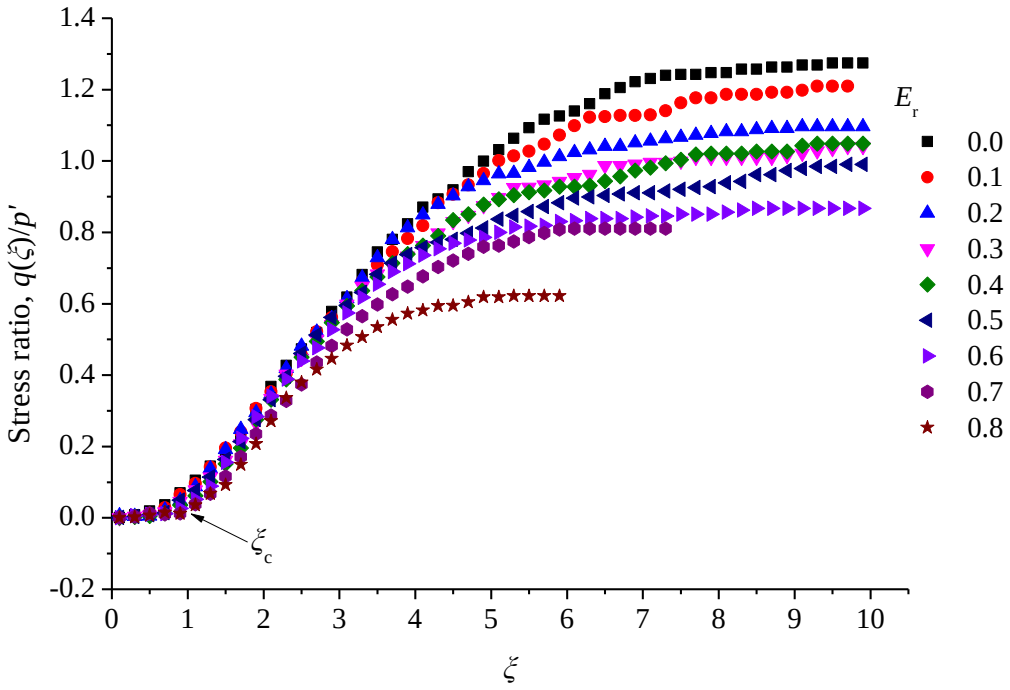

Fig. 12. Cumulative stress ratio $q(\xi)/p'$ as a function of ξ at ε_1=50% for different E_r.

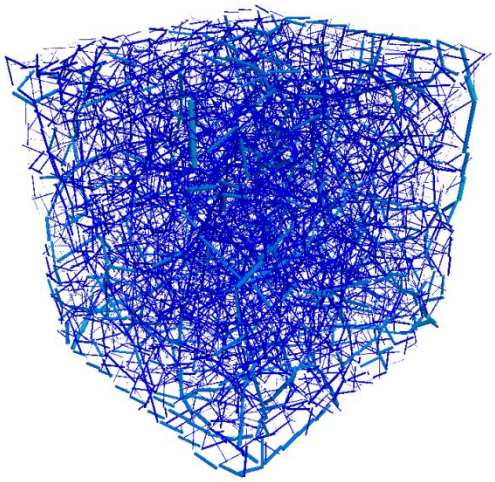

(a)

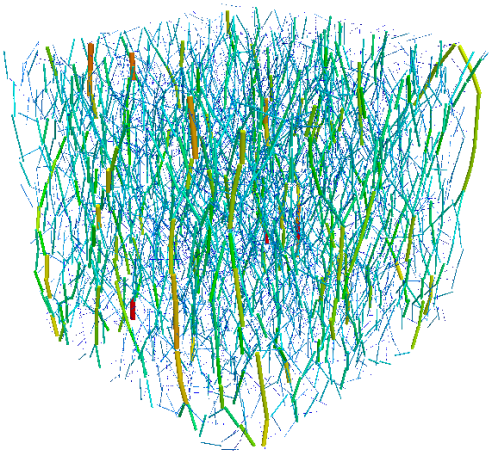

(b)

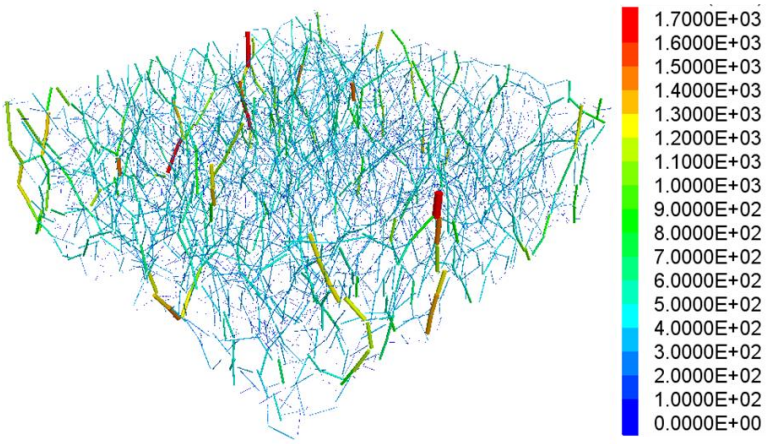

(c)

Fig. 13. Maps of normal contact force at initial (a), peak (b) and critical (c) states for the assembly with E_r=0.4. The line thickness is proportional to the magnitude of the normal contact force.

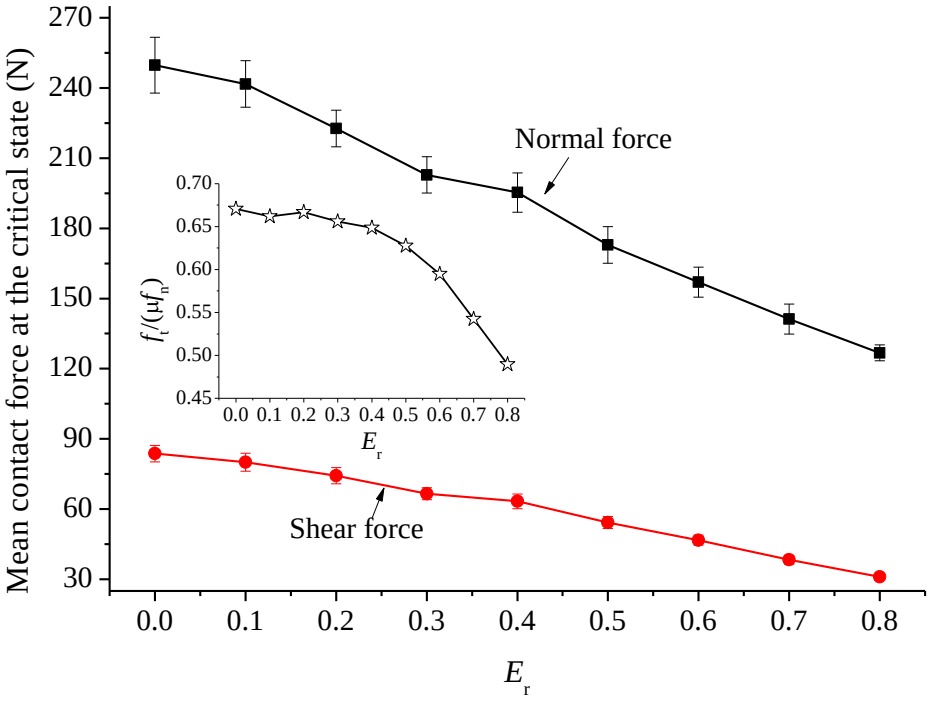

Fig. 14. Mean normal and shear contact forces at the critical state; error bars display the deviation of contact forces at the critical state. The inset shows the ratio of f_t to μf_n versus E_r.

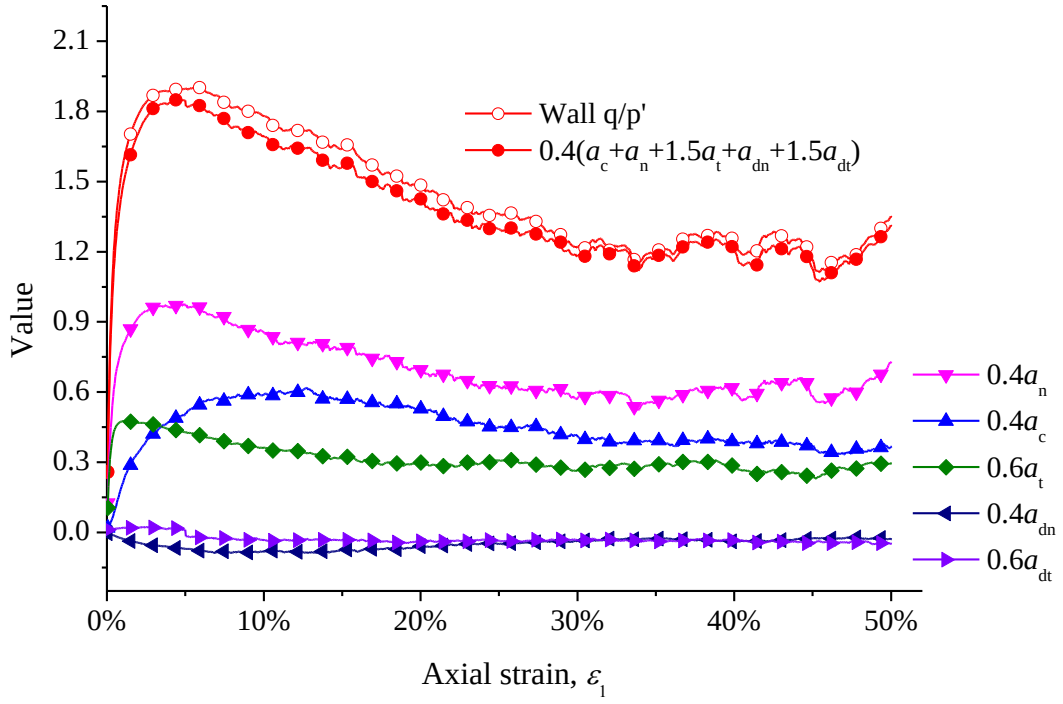

(a)

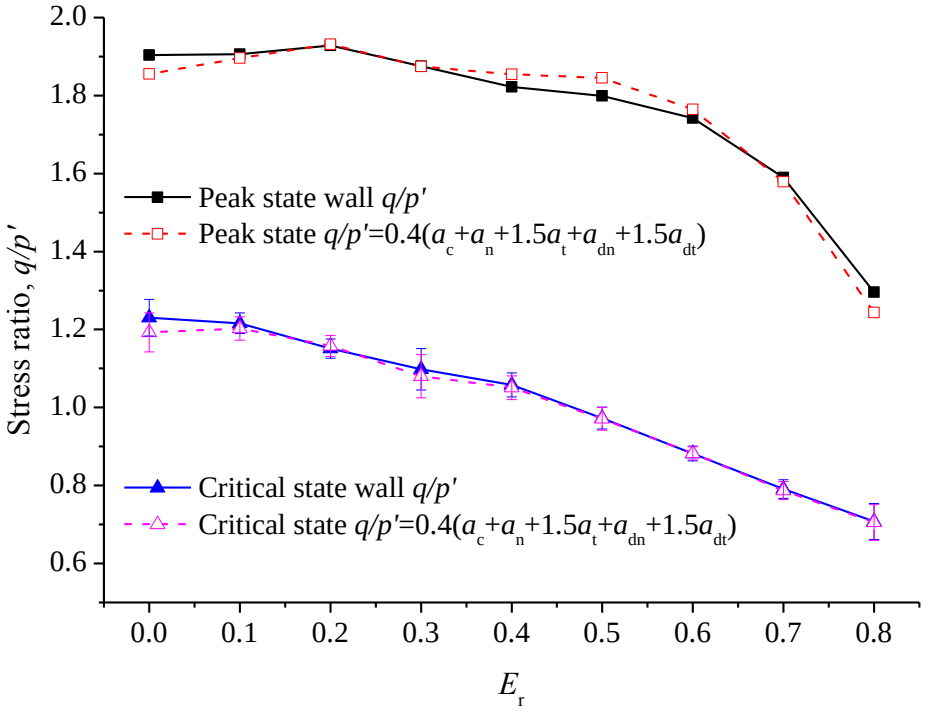

(b)

Fig. 15. Validating the SFF relationship: (a) evolution of the effective stress ratio q/p' and anisotropies with axial strain for E_r=0.0 and (b) evolution of q/p' at the peak and critical states with different roundness along with the analytical expression given in Eq. (10); error bars denote the standard deviation at the critical state.

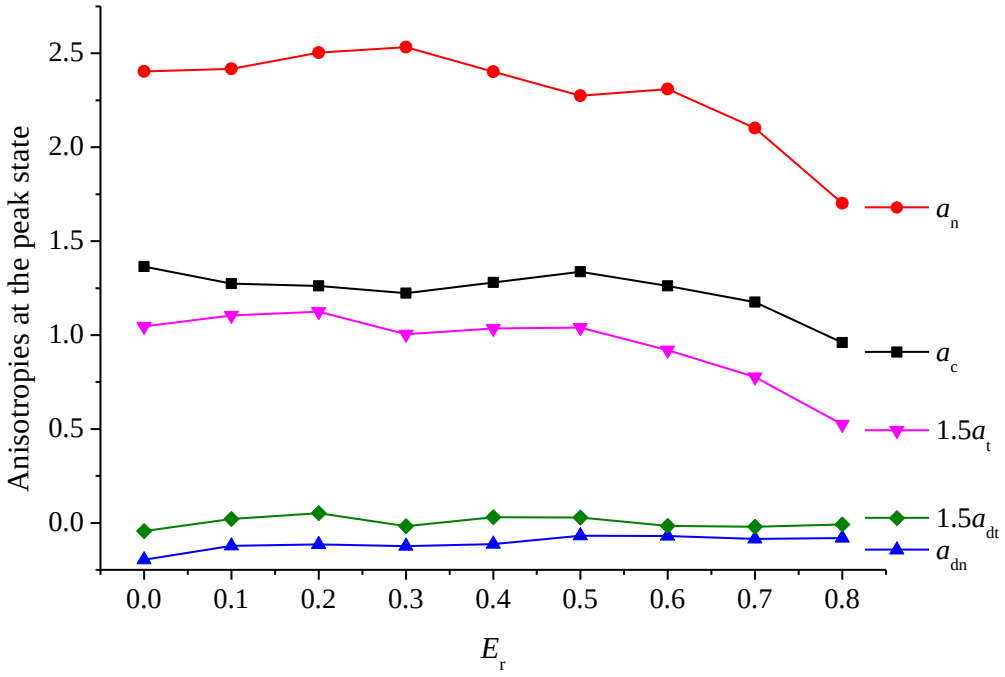

(a)

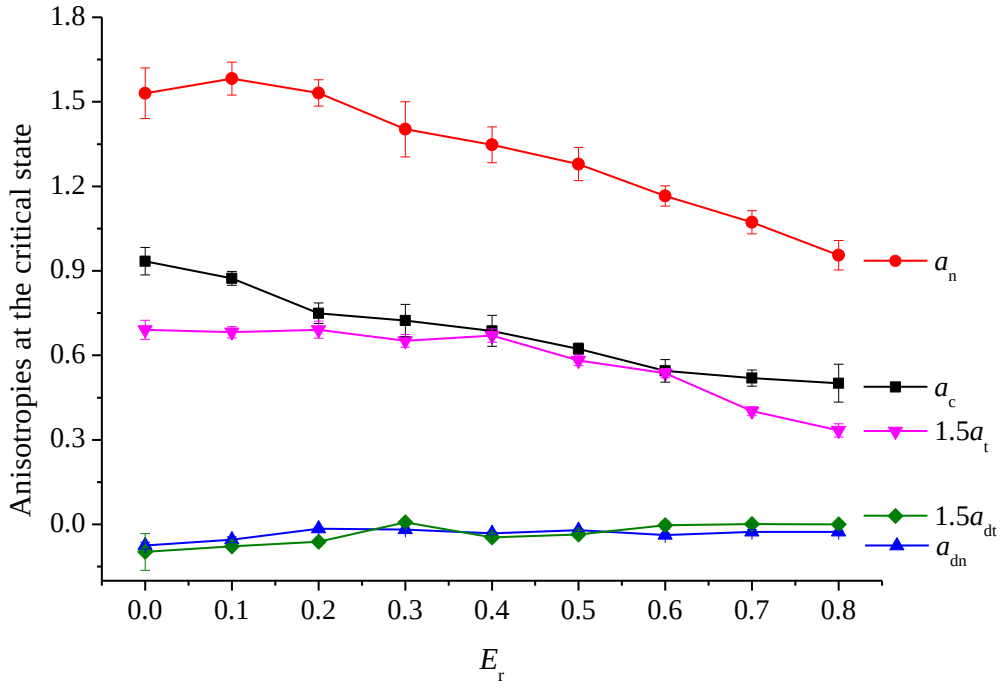

(b)

Fig. 16. Variation in anisotropic coefficients (i.e., a_c, a_n, $1.5a_t$, a_{dn} and $1.5a_{dt}$) with varying E_r at the (a) peak state and (b) critical state.

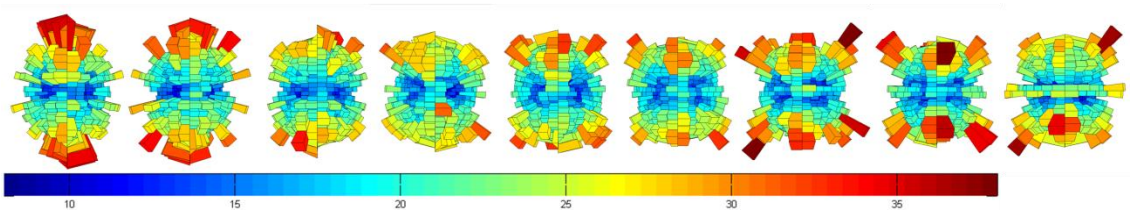

(a)

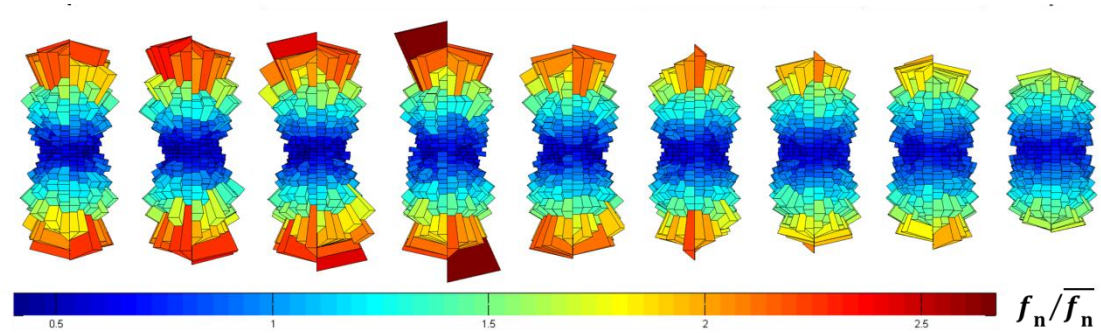

(b)

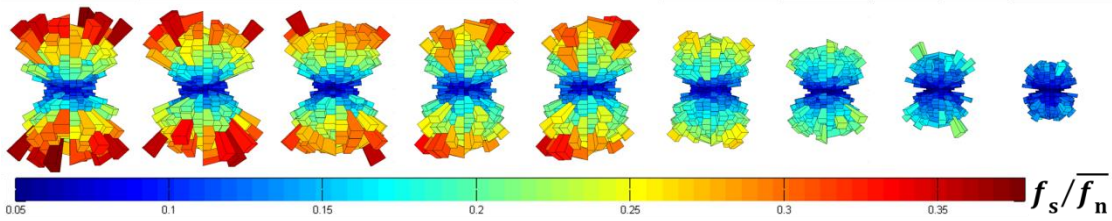

(c)

Fig. 17. Rose diagrams of (a) the contact number, (b) contact normal force (CNF) and (c) contact shear force (CSF) for all assemblies at the critical state. From left to right, rose diagrams represent the evolution of E_r from 0.0 to 0.8.

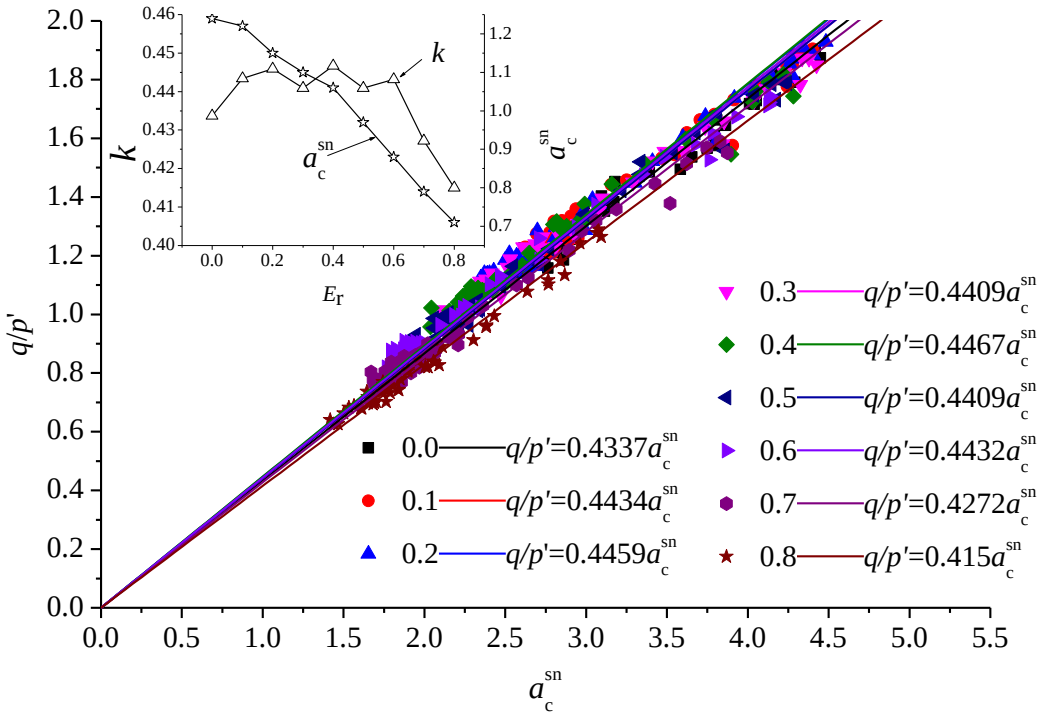

Fig. 18. Linear relationship between the macroscopic stress ratio and the anisotropy within a strong and non-sliding contact a_c^{sn}. The inset illustrates the evolutions of k and a_c^{sn} at the critical state with E_r.